EXOPLANETS

A nearby transiting rocky exoplanet that is suitable for atmospheric investigation

T. Trifonov[1]*, J. A. Caballero[2], J. C. Morales[3,4], A. Seifahrt[5], I. Ribas[3,4], A. Reiners[6], J. L. Bean[5], R. Luque[7,8], H. Parviainen[7,8], E. Pallé[7,8], S. Stock[9], M. Zechmeister[6], P. J. Amado[10], G. Anglada-Escudé[3,4], M. Azzaro[11], T. Barclay[12,13], V. J. S. Béjar[7,8], P. Bluhm[9], N. Casasayas-Barris[7,8], C. Cifuentes[2], K. A. Collins[14], K. I. Collins[15], M. Cortés-Contreras[2], J. de Leon[16], S. Dreizler[6], C. D. Dressing[17], E. Esparza-Borges[7,8], N. Espinoza[18], M. Fausnaugh[19], A. Fukui[20,7], A. P. Hatzes[21], C. Hellier[22], Th. Henning[1], C. E. Henze[23], E. Herrero[3,4], S. V. Jeffers[6,24], J. M. Jenkins[23], E. L. N. Jensen[25], A. Kaminski[9], D. Kasper[5], D. Kossakowski[1], M. Kürster[1], M. Lafarga[3,4], D. W. Latham[14], A. W. Mann[26], K. Molaverdikhani[9], D. Montes[27], B. T. Montet[28], F. Murgas[7,8], N. Narita[29,30,31,7], M. Oshagh[7,8], V. M. Passegger[32,33], D. Pollacco[34], S. N. Quinn[14], A. Quirrenbach[9], G. R. Ricker[19], C. Rodríguez López[10], J. Sanz-Forcada[2], R. P. Schwarz[35], A. Schweitzer[32], S. Seager[19,36,37], A. Shporer[19], M. Stangret[7,8], J. Stürmer[9], T. G. Tan[38], P. Tenenbaum[19], J. D. Twicken[39,23], R. Vanderspek[19], J. N. Winn[40]

Spectroscopy of transiting exoplanets can be used to investigate their atmospheric properties and habitability. Combining radial velocity (RV) and transit data provides additional information on exoplanet physical properties. We detect a transiting rocky planet with an orbital period of 1.467 days around the nearby red dwarf star Gliese 486. The planet Gliese 486 b is 2.81 Earth masses and 1.31 Earth radii, with uncertainties of 5%, as determined from RV data and photometric light curves. The host star is at a distance of ~8.1 parsecs, has a *J*-band magnitude of ~7.2, and is observable from both hemispheres of Earth. On the basis of these properties and the planet's short orbital period and high equilibrium temperature, we show that this terrestrial planet is suitable for emission and transit spectroscopy.

The combination of transit photometry and Doppler radial velocity (RV) measurements can determine precise values of the masses, radii, bulk densities, and surface gravities of exoplanets. Determination of an exoplanet's atmospheric properties is possible using transmission and emission spectroscopy, but doing so for rocky exoplanets is challenging because of their small size. The CARMENES (Calar Alto high-Resolution search for M dwarfs with Exo-earths with Near-infrared and optical Echelle spectrographs) survey (*1*) and the Transiting Exoplanet Survey Satellite (TESS) mission (*2*) together have the sensitivity required to detect and, potentially, jointly investigate and characterize nearby exoplanet systems. Small exoplanets are easier to detect around red dwarfs (main-sequence stars of spectral type M), as those stars are themselves small and of low mass. Particularly important are small, Earth-sized terrestrial planets in the habitable zone (*3*, *4*), the region where liquid water could exist on the surface. The orbital periods expected for terrestrial planets in the habitable zone around M dwarfs are a few tens of days, and the predicted RV signals are large enough to be detectable.

M dwarfs are abundant in the Solar neighborhood; of the 357 cataloged main-sequence stars within 10 pc of the Sun, 283 (79%) are of type M (*5*, *6*). Nearby exoplanets are favored for follow-up characterization, mainly because of their brighter host stars (producing a higher signal-to-noise ratio). Within 10 pc, ~80 planets in 40 stellar systems are known, of which ~50 planets orbit around 35 M dwarf hosts. These include the closest exoplanet systems, such as Proxima Centauri (*7*, *8*) and Barnard's star (*9*).

We observed the nearby star Gliese 486 [Wolf 437, TESS Object of Interest (TOI) 1827], a red dwarf of spectral type M3.5 V, as one of the ~350 targets in the CARMENES survey (*10*). RV monitoring of the star between 2016 and early 2020 showed a periodicity of 1.467 days with a false-alarm probability of <0.1% (*11*). No counterpart was found in stellar activity indices, suggesting that the signal was due to an orbiting planet rather than stellar variability, which is common in M dwarfs. We used photometric data from TESS to confirm the presence of the planet, identifying 13 transit events with a periodicity of 1.467 days (*11*). At a distance of 8.1 pc, Gliese 486 is the third-closest transiting exoplanet system known, and Gliese

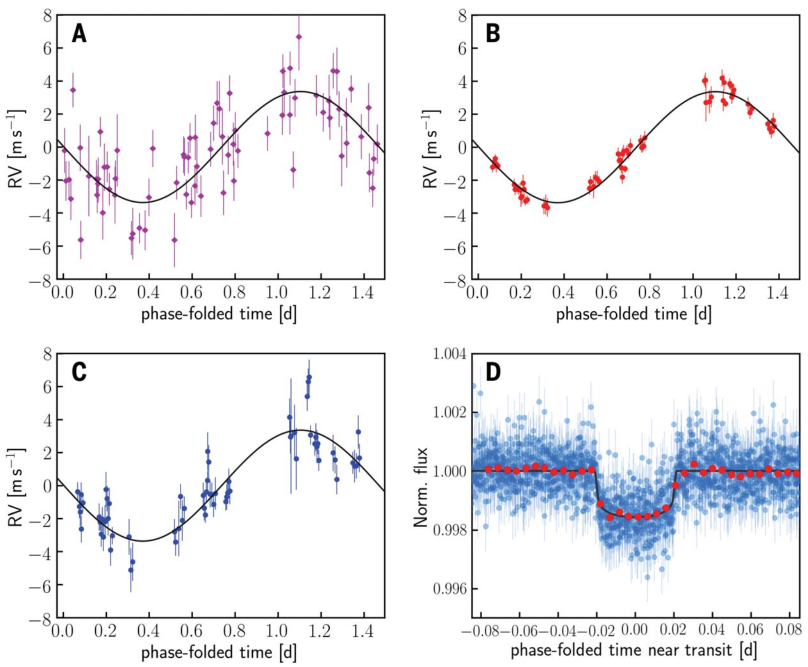

Fig. 1. Radial velocity and light curves of Gliese 486. Phase-folded RV data from (**A**) CARMENES VIS, (**B**) MAROON-X red, and (**C**) MAROON-X blue, and (**D**) *TESS* photometric data. Blue circles in (D) represent the phase-folded 2-min cadence TESS transit photometry, whereas red circles are 1-hour bins of the phase-folded data. Error bars indicate 1σ uncertainties of individual measurements. Black solid curves in all panels are the maximum likelihood orbital model from a joint fitting of all these data simultaneously. Norm. flux, normalized flux; d, days.

486 b is the closest transiting planet around a red dwarf with a measured mass.

We list the physical properties of the star Gliese 486 and planet Gliese 486 b in Table 1 (*11*). From the CARMENES spectroscopic observations and a photometric data compilation (*12*), we computed a stellar radius of 0.328 ± 0.011 solar radii ($R_\odot$) and a mass of 0.323 ± 0.015 solar masses ($M_\odot$) following (*13*). Because of its closeness, Gliese 486 has been a target of direct-imaging exoplanet searches (*14*, *15*), which placed upper limits on low-mass stellar and substellar companions at sky-projected physical separations between 1.2 and 161 astronomical units (au), larger than the orbit we find for Gliese 486 b.

Table 1. Measured properties of Gliese 486 and its planet. We used gravitational constant G = 6.67430 10^{-11} m^3 kg^{-1} s^{-2}, $M_\odot$ = 1.98847 10^{30} kg, $R_\odot$ = 6.957 10^8 m, M_E = 5.9722 10^{24} kg, and R_E = 6.3781 10^6 m. The tabulated rotation period is a proxy obtained from a quasi-periodic representation of the photometric variability. The eccentricity upper limit of <0.05 is constrained at the 68.3% confidence level. The tabulated equilibrium temperature would be 60 K cooler if the Bond albedo were 0.30.

Parameters	Value
Stellar	
Right ascension (J2000 equinox)	12:47:56.62
Declination (J2000 equinox)	+09:45:05.0
Spectral type	M3.5 ± 0.5 V
J-band magnitude (mag)	7.195 ± 0.026
Mass ($M_\odot$)	0.323 ± 0.015
Radius ($R_\odot$)	0.328 ± 0.011
Luminosity ($L_\odot$)	0.01210 ± 0.00023
Effective temperature (K)	3340 ± 54
Distance (pc)	8.0761 ± 0.0041
Rotation period (days)	$130.1^{+1.6}_{-1.2}$
Metallicity [Fe/H] (dex)	+0.07 ± 0.16
Planetary	
Orbital period (days)	$1.467119^{+0.000031}_{-0.000030}$
Radial velocity semiamplitude (m s^{-1})	$3.370^{+0.078}_{-0.080}$
Eccentricity	<0.05
Argument of periastron (degrees)	unconstrained
Time of inferior transit (barycentric Julian date)	$2,458,931.15935^{+0.00042}_{-0.00042}$
Orbital semimajor axis (au)	$0.01734^{+0.00026}_{-0.00027}$
Mass (M_E)	$2.82^{+0.11}_{-0.12}$
Radius (R_E)	$1.305^{+0.063}_{-0.067}$
Inclination (degrees)	$88.4^{+1.1}_{-1.4}$
Insolation (S_E)	$40.3^{+1.5}_{-1.4}$
Mean density (10^{-3} kg m^{-3})	$7.0^{+1.2}_{-1.0}$
Surface gravitational acceleration (m s^{-2})	$16.4^{+0.6}_{-0.5}$
Equilibrium temperature (K)	701^{+13}_{-13}

We supplemented the TESS photometry with ground-based photometric monitoring and archival time series data to further characterize the transit events and determine the stellar rotation period. Using photometry of Gliese 486 collected by the Wide Angle Search for Planets (WASP) (*16*) between 2008 and 2014 and by the All-Sky Automated Survey for Supernovae (ASAS-SN) (*17*) between 2012 and 2020, we measured a stellar rotation period $P_{rot} = 130.1^{+1.6}_{-1.2}$ days, which is consistent with our expectations for an old and weakly active M-dwarf star and much longer than the planet orbital period (fig. S4). We observed two additional transit events using the Multicolor Simultaneous Camera for studying Atmospheres of Transiting exoplanets 2 (MuSCAT2) (*18*) at the 1.5-m Telescopio Carlos Sánchez at Observatorio del Teide on 9 May 2020 and 12 May 2020 and three more transits with the 1.0-m Las Cumbres Observatory Global Telescope (LCOGT) (*19*) at Siding Spring Observatory on 15 May 2020, 24 May 2020, and 5 June 2020.

We complemented our CARMENES RV observations of Gliese 486 with data from the M-dwarf Advanced Radial velocity Observer Of Neighboring eXoplanets (MAROON-X) spectrograph (*20*) at the 8.1-m Gemini North telescope. In total, we obtained 80 CARMENES spectra between 2016 and 2020 and 65 with MAROON-X between May and June 2020. These data provide complete phase coverage of the Gliese 486 b RV signal (Fig. 1), with a total weighted root mean square residual of 1.05 m s^{-1}.

We performed an orbital analysis using the Exo-Striker software (*21*). Global parameter

[1]Max-Planck-Institut für Astronomie, D-69117 Heidelberg, Germany. [2]Centro de Astrobiología (Consejo Superior de Investigaciones Científicas – Instituto Nacional de Técnica Aeroespacial), E-28692 Villanueva de la Cañada, Madrid, Spain. [3]Institut de Ciències de l'Espai (Consejo Superior de Investigaciones Científicas), E-08193 Bellaterra, Barcelona, Spain. [4]Institut d'Estudis Espacials de Catalunya, E-08034 Barcelona, Spain. [5]Department of Astronomy and Astrophysics, University of Chicago, Chicago, IL 60637, USA. [6]Institut für Astrophysik, Georg-August-Universität, D-37077 Göttingen, Germany. [7]Instituto de Astrofísica de Canarias, E-38205 La Laguna, Tenerife, Spain. [8]Departamento de Astrofísica, Universidad de La Laguna, E-38206 La Laguna, Tenerife, Spain. [9]Landessternwarte, Zentrum für Astronomie der Universität Heidelberg, D-69117 Heidelberg, Germany. [10]Instituto de Astrofísica de Andalucía (Consejo Superior de Investigaciones Científicas), E-18008 Granada, Spain. [11]Centro Astronómico Hispano-Alemán, Observatorio de Calar Alto, E-04550 Gérgal, Almería, Spain. [12]NASA Goddard Space Flight Center, Greenbelt, MD 20771, USA. [13]University of Maryland, Baltimore County, Baltimore, MD 21250, USA. [14]Center for Astrophysics, Harvard & Smithsonian, Cambridge, MA 02138, USA. [15]Department of Physics and Astronomy, George Mason University, Fairfax, VA 22030, USA. [16]Department of Astronomy, Graduate School of Science, University of Tokyo, Tokyo 113-0033, Japan. [17]Astronomy Department, University of California at Berkeley, Berkeley, CA 94720, USA. [18]Space Telescope Science Institute, Baltimore, MD 21218, USA. [19]Department of Physics and Kavli Institute for Astrophysics and Space Research, Massachusetts Institute of Technology, Cambridge, MA 02139, USA. [20]Department of Earth and Planetary Science, Graduate School of Science, University of Tokyo, Tokyo 113-0033, Japan. [21]Thüringer Landessternwarte Tautenburg, D-07778 Tautenburg, Germany. [22]Astrophysics Group, Keele University, Staffordshire ST5 5BG, UK. [23]NASA Ames Research Center, Moffett Field, CA 94035, USA. [24]Max-Planck-Institut für Sonnensystemforschung, D-37077, Göttingen, Germany. [25]Department of Physics and Astronomy, Swarthmore College, Swarthmore, PA 19081, USA. [26]Department of Physics and Astronomy, University of North Carolina at Chapel Hill, Chapel Hill, NC 27599, USA. [27]Departamento de Física de la Tierra y Astrofísica and Instituto de Física de Partículas y del Cosmos, Facultad de Ciencias Físicas, Universidad Complutense de Madrid, E-28040 Madrid, Spain. [28]School of Physics, University of New South Wales, Sydney NSW 2052, Australia. [29]Komaba Institute for Science, University of Tokyo, Tokyo 153-8902, Japan. [30]Japan Science and Technology Agency, Precursory Research for Embryonic Science and Technology, Tokyo 153-8902, Japan. [31]Astrobiology Center, Tokyo 181-8588, Japan. [32]Hamburger Sternwarte, Universität Hamburg, D-21029 Hamburg, Germany. [33]Homer L. Dodge Department of Physics and Astronomy, University of Oklahoma, Norman, OK 73019, USA. [34]Department of Physics, University of Warwick, Coventry CV4 7AL, UK. [35]Patashnick Voorheesville Observatory, Voorheesville, NY 12186, USA. [36]Department of Earth, Atmospheric and Planetary Sciences, Massachusetts Institute of Technology, Cambridge, MA 02139, USA. [37]Department of Aeronautics and Astronautics, Massachusetts Institute of Technology, Cambridge, MA 02139, USA. [38]Perth Exoplanet Survey Telescope, Perth WA 6010, Australia. [39]Search for Extraterrestrial Intelligence Institute, Mountain View, CA 94043, USA. [40]Department of Astrophysical Sciences, Princeton University, Princeton, NJ 08544, USA.
***Corresponding author. Email: trifonov@mpia.de**

Fig. 2. Mass-radius diagram for known transiting planets with measured masses between 0.5 and 5.5 M_E and radii between 0.5 and 2.0 R_E. We show all cases with precision better than 30% (see supplementary text). Gliese 486 b is shown in red, planets orbiting around late-type stars with T_{eff} < 4000 K are shown in orange, and hotter stars are shown in dark gray. Earth (blue circle with cross) and Venus (light gray circle with ♀ symbol) are shown for comparison. Curves show theoretical planet mass-radius relationships for compositions indicated in the legend: pure water (H_2O), pure enstatite ($MgSiO_3$) rock, an Earth-like mixture of 50% enstatite and 50% iron, and pure iron (Fe) (*23*).

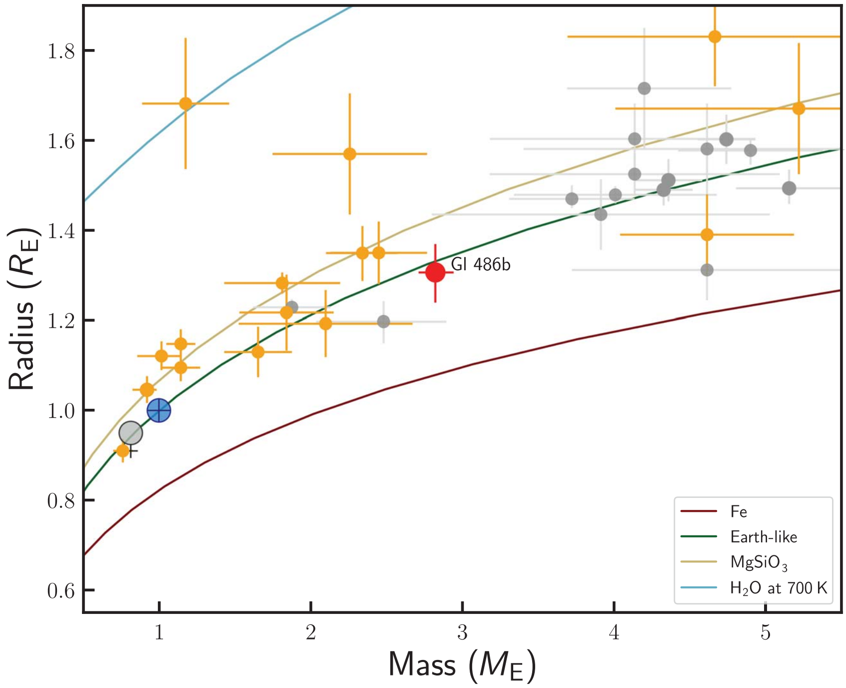

Fig. 3. Metrics for transmission and emission spectroscopy for rocky planets with measured masses orbiting nearby M dwarfs. (**A**) Expected primary transit transmission signal per scale height as a function of K_s-band magnitude. Gliese 486 b is shown with a star, planets around bright G and K dwarfs at a distance of <30 pc are shown with open circles, and planets around M dwarfs are shown with solid circles. The color bar indicates the planet radius. Selected planets are labeled. (**B**) Same as (A), but for the transmission spectroscopy metric (computed homogeneously with a scale factor 0.190) as a function of T_{eq}. (**C**) Same as (A), but for the emission spectroscopy metric as a function of T_{eq}. In (A), diagonal dashed lines mark expected amplitudes of spectral features in transmission at three different, arbitrary exposure times t_{exp}, 2 t_{exp}, and 3 t_{exp} with the same instrumental setup. In (B) and (C), planets hotter than the vertical lines at T_{eq} = 880 K are expected to have molten lava surfaces. See supplementary text for details.

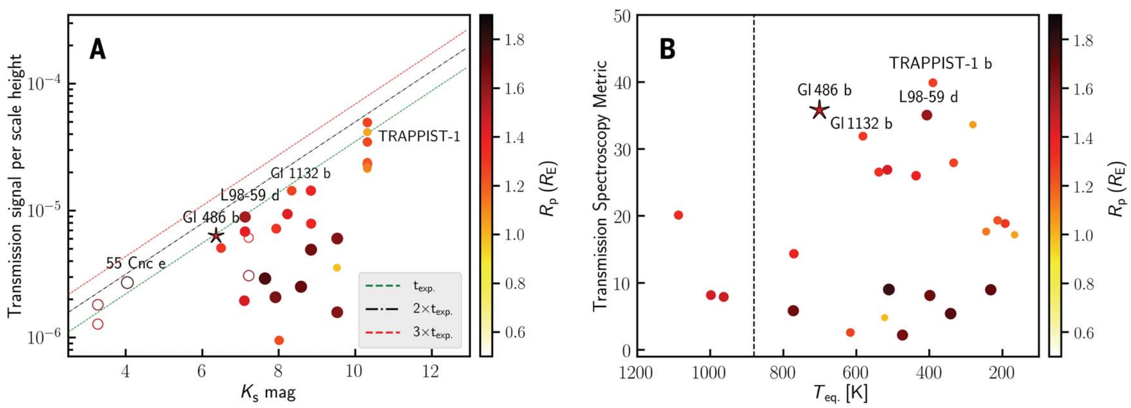

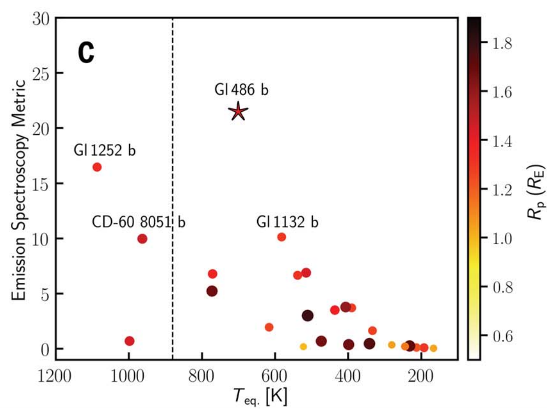

optimization was performed by simultaneously fitting Keplerian orbit models to the CARMENES visual channel (VIS), MAROON-X red and blue channels, and the TESS photometry. An alternative model that also includes transit data from MuSCAT2 and LCOGT provides consistent results (*11*). For Gliese 486 b, we obtained a planet orbital period P_b = $1.467119^{+0.000031}_{-0.000030}$ days and an orbital inclination i_b = $88.4^{+1.1}_{-1.4}$

degrees. Using the RV semiamplitude $K_b = 3.37^{+0.08}_{-0.08}$ m s^{-1}, the stellar parameters of Gliese 486, and the orbital parameters, we derived a dynamical planet mass $M_b = 2.82^{+0.11}_{-0.12}$ Earth masses (M_E), a semimajor axis $a_b = 0.01732^{+0.00027}_{-0.00027}$ au, and a planet radius $R_b = 1.306^{+0.063}_{-0.067}$ Earth radii (R_E). We concluded that Gliese 486 b has a circular orbit with an upper limit on the eccentricity $e_b < 0.05$ at a 68.3% confidence level. This low eccentricity is consistent with the short orbital period, as star-planet tidal forces would act to circularize the orbit. We performed star-planet tidal simulations of the Gliese 486 system with the EqTide integrator (*22*) and found that the orbit of Gliese 486 b becomes fully circularized within ~1 million years.

From the planet mass and radius, we derived a planet bulk density $\rho_b = 7.0^{+1.2}_{-1.0}\ 10^{-3}$ kg m^{-3} (~1.3 times that of Earth) and a surface gravity $g_b = 16.2^{+1.9}_{-1.6}$ m s^{-2} (~1.7 times that of Earth), respectively. From the location of Gliese 486 b in a radius-mass diagram (Fig. 2), its density indicates an iron-to-silicate ratio similar to Earth's (*23*). The inferred mass and radius of ~2.82 M_E and ~1.31 R_E put Gliese 486 b at the boundary between Earth and super-Earth planets (*24*), but the bulk density indicates a massive terrestrial planet rather than an ocean planet (*25*). The escape velocity at 1 R_b is $v_e = 16.4^{+0.6}_{-0.5}$ km s^{-1}. For an energy-limited atmospheric escape model (*26*) and the previously measured host star x-ray flux upper limit (*27*), we derive a low photoevaporation rate of $\dot{M}_{\rm phot} < 10^7\,{\rm g\,s^{-1}}$. From the stellar bolometric luminosity and the planet semimajor axis, we inferred a planet irradiance S_b of $40.3^{+1.5}_{-1.4}$ times that of Earth. Assuming complete absorbance (a Bond albedo $A_B = 0$), this equates to an equilibrium temperature $T_{eq} = 701^{+13}_{-13}$ K, which is slightly cooler than that of Venus.

Figure 3 shows how Gliese 486 b compares with other possibly rocky planets around nearby M dwarfs (those with measured masses and radii $R_p < 2.0\ R_E$) using standard metrics for transmission and emission spectroscopy. Figure 3A shows the expected primary transit transmission signal δ per atmospheric scale height H ($\delta \approx 2HR_p/R_\star^2$, where R_p is the radius of the planet, and $R_\star$ is the radius of the star) as a function of apparent magnitude in the K_s band. Figure 3B shows the transmission spectroscopy metric as a function of T_{eq}, whereas panel Fig. 3C shows the emission spectroscopy metric, which is the signal-to-noise ratio expected for a single secondary eclipse observation by the James Webb Space Telescope (*28*). Figure 3, B and C, show planets around M dwarfs with measured masses. With a radius of 1.31 R_E, Gliese 486 b is located well below the radius range of 1.4 to 1.8 R_E, under which planets are expected to have lost their primordial hydrogen-helium atmospheres owing to photoevaporation processes (*29*). It remains unknown how stellar irradiation and planet surface gravity affect the formation and retention of secondary atmospheres. Planets with T_{eq} > 880 K, such as 55 Cancri e (*30*), are expected to have molten (lava) surfaces and no atmospheres, except for vaporized rock (*31*). Gliese 486 b is not hot enough to be a lava world, but its temperature of ~700 K makes it suitable for emission spectroscopy and phase curve studies in search of an atmosphere (*28*). Our orbital model constrains the secondary eclipse time to within 13 min (at 1σ uncertainty), which is necessary for efficient scheduling of observations. Compared with other known nearby rocky planets around M dwarfs, Gliese 486 b has a shorter orbital period and correspondingly higher equilibrium temperature of ~700 K and orbits a brighter, cooler, and less active stellar host.

REFERENCES AND NOTES

1. A. Quirrenbach *et al.*, *Proc. SPIE Int. Soc. Opt. Eng.* **9908**, 990812 (2016).
2. G. R. Ricker *et al.*, *J. Astron. Telesc. Instrum. Syst.* **1**, 014003 (2015).
3. J. F. Kasting, D. P. Whitmire, R. T. Reynolds, *Icarus* **101**, 108–128 (1993).
4. J. C. Tarter *et al.*, *Astrobiology* **7**, 30–65 (2007).
5. I. N. Reid, J. E. Gizis, S. L. Hawley, *Astron. J.* **124**, 2721–2738 (2002).
6. T. J. Henry *et al.*, *Astron. J.* **132**, 2360–2371 (2006).
7. G. Anglada-Escudé *et al.*, *Nature* **536**, 437–440 (2016).
8. M. Damasso *et al.*, *Sci. Adv.* **6**, eaax7467 (2020).
9. I. Ribas *et al.*, *Nature* **563**, 365–368 (2018).
10. A. Reiners *et al.*, *Astron. Astrophys.* **612**, A49 (2018).
11. Materials and methods are available as supplementary materials.
12. C. Cifuentes *et al.*, *Astron. Astrophys.* **642**, A115 (2020).
13. A. Schweitzer *et al.*, *Astron. Astrophys.* **625**, A68 (2019).
14. S. B. Dieterich, T. J. Henry, D. A. Golimowski, J. E. Krist, A. M. Tanner, *Astron. J.* **144**, 64 (2012).
15. K. Ward-Duong *et al.*, *Mon. Not. R. Astron. Soc.* **449**, 2618–2637 (2015).
16. D. L. Pollacco *et al.*, *Publ. Astron. Soc. Pac.* **118**, 1407–1418 (2006).
17. B. J. Shappee *et al.*, *Astrophys. J.* **788**, 48 (2014).
18. N. Narita *et al.*, *J. Astron. Telesc. Instrum. Syst.* **5**, 015001 (2018).
19. T. M. Brown *et al.*, *Publ. Astron. Soc. Pac.* **125**, 1031–1055 (2013).
20. A. Seifahrt, J. Stürmer, J. L. Bean, C. Schwab, *Proc. SPIE Int. Soc. Opt. Eng.* **10702**, 107026D (2018).
21. T. Trifonov, The Exo-Striker: Transit and radial velocity interactive fitting tool for orbital analysis and N-body simulations, Astrophysics Source Code Library, record ascl:1906.004 (2019).
22. R. Barnes, *Celestial Mech. Dyn. Astron.* **129**, 509–536 (2017).
23. L. Zeng *et al.*, *Proc. Natl. Acad. Sci. U.S.A.* **116**, 9723–9728 (2019).
24. H. J. van Heck, P. J. Tackley, *Earth Planet. Sci. Lett.* **310**, 252–261 (2011).
25. D. Valencia, D. D. Sasselov, R. J. O'Connell, *Astrophys. J.* **665**, 1413–1420 (2007).
26. J. Sanz-Forcada *et al.*, *Astron. Astrophys.* **532**, A6 (2011).
27. B. Stelzer, A. Marino, G. Micela, J. López-Santiago, C. Liefke, *Mon. Not. R. Astron. Soc.* **431**, 2063–2079 (2013).
28. E. M. R. Kempton *et al.*, *Publ. Astron. Soc. Pac.* **130**, 114401 (2018).
29. B. J. Fulton *et al.*, *Astron. J.* **154**, 109 (2017).
30. B. E. McArthur *et al.*, *Astrophys. J.* **614**, L81–L84 (2004).
31. M. Mansfield *et al.*, *Astrophys. J.* **886**, 141 (2019).

ACKNOWLEDGMENTS

This work was based on observations made with the CARMENES spectrograph at the 3.5-m telescope of the Centro Astronómico Hispano-Alemán de Calar Alto (CAHA, Almería, Spain), funded by the German Max-Planck-Gesellschaft (MPG), the Spanish Consejo Superior de Investigaciones Científicas (CSIC), the European Regional Development Fund, and the CARMENES consortium members and stored at the CARMENES data archive at CAB (INTA-CSIC); the MAROON-X spectrograph, which was funded by the David and Lucile Packard Foundation, the Heising-Simons Foundation, the Gemini Observatory, and the University of Chicago (the MAROON-X team thanks the staff of the Gemini Observatory for their assistance with the commissioning and operation of the instrument); the LCOGT network; the MuSCAT2 instrument, developed by the Astrobiology Center, at Telescopio Carlos Sánchez operated on the island of Tenerife by the Instituto de Astrofísica de Canarias in the Spanish Observatorio del Teide; and data collected by the TESS mission. **Funding:** Funding was provided by Deutsche Forschungsgemeinschaft through research unit FOR2544 "Blue Planets around Red Stars" and priority program SPP1992 "Exploring the Diversity of Extrasolar Planets"; Agencia Estatal de Investigación of the Ministerio de Ciencia e Innovación and the European Regional Development Fund through projects PID2019-109522GB-C51/2/3/4, PGC2018-098153-B-C33, SEV-2017-0709, MDM-2017-0737, AYA2016-79425-C3-1/2/3-P, ESP2016-80435-C2-1-R, and SEV-2015-0548; Klaus Tschira Stiftung; European Union's Horizon 2020 through Marie Sklodowska Curie grant 713673; "la Caixa" through INPhINT grant LCF/BQ/IN17/1162033; NASA through grants NNX17AG24G, 80NSSC19K0533, 80NSSC19K1721, and 80NSSC18K158 and the NASA Science Mission Directorate; Japan Society for the Promotion of Science KAKENHI through grants JP17H04574, JP18H01265, and JP18H05439; and Japan Science and Technology Agency PRESTO through grant JPMJPR1775. **Author contributions:** T.T. analyzed and interpreted the data and wrote the manuscript. J.A.C. is the CARMENES instrument astronomer and helped write the manuscript. J.C.M. scheduled the CARMENES observations and performed preliminary CARMENES RV analysis and transit predictions. I.R. and A.R. are the CARMENES project scientists and identified the periodic radial velocity signal. J.L.B., R.L., E.P., S.St., and K.M. contributed to writing the manuscript. A.Se. and M.Z. reduced the CARMENES and MAROON-X spectra. G.A.-E., P.B., N.E., and A.P.H. analyzed the RV and photometric time series. C.C., M.C.-C., V.M.P., J.S.-F., and A.Sc. determined stellar parameters. The following authors contributed to instrument operations, science coordination, and data analysis: P.J.A., M.A., V.J.S.B., S.D., T.H., S.V.J., A.K., D.Ko., M.K., M.L., D.M., A.Q., and C.R.L. for CARMENES; D.Ka., B.T.M., and J.S. for MAROON-X; N.C.-B., J.d.L., E.E.-B., A.F., F.M., N.N., H.P., and M.S. for MuSCAT2; K.A.C., K.I.C., E.L.N.J., A.Sh., and R.P.S. for LCOGT; C.H., E.H., D.P., and T.G.T. for PEST, TJO, and SuperWASP; T.B., C.D.D., M.F., C.E.H., J.M.J., D.W.L., A.W.M., S.N.Q., G.R.R., S.Se., P.T., J.D.T., R.V., and J.N.W. for TESS. **Competing interests:** The authors declare no competing interests. **Data and materials availability:** All time series data used (RV, activity indices, and light curves from CARMENES, MAROON-X, HARPS, HIRES, MuSCAT2, LCOGT, SuperWASP, ASAS-SN, TJO, and TESS) are available at the Centro de Astrobiología CARMENES data archive http://carmenes.cab.inta-csic.es/ as machine-readable tables. The derived RVs and light curves are provided in tables S1 to S4 and data S1. The Exo-Striker code is available at https://github.com/3fon3fonov/exostriker, the Juliet code at https://github.com/nespinoza/juliet, and the EqTide code at https://github.com/RoryBarnes/EqTide.

SUPPLEMENTARY MATERIALS

science.sciencemag.org/content/371/6533/1038/suppl/DC1
Materials and Methods
Supplementary Text
Figs. S1 to S10
Tables S1 to S6
References (*32–102*)
Data S1

10 July 2020; accepted 2 February 2021
10.1126/science.abd7645